analytical chemistry

pubs.acs.org/ac Article

Simultaneous Optical Photothermal Infrared (O-PTIR) and Raman Spectroscopy of Submicrometer Atmospheric Particles

Nicole E. Olson, Yao Xiao, Ziying Lei, and Andrew P. Ault*

Cite This: *Anal. Chem.* 2020, 92, 9932−9939 Read Online

ACCESS | Metrics & More | Article Recommendations | Supporting Information

ABSTRACT: Physicochemical analysis of individual atmospheric aerosols at the most abundant sizes in the atmosphere (<1 μm) is analytically challenging, as hundreds to thousands of species are often present in femtoliter volumes. Vibrational spectroscopies, such as infrared (IR) and Raman, have great potential for probing functional groups in single particles at ambient pressure and temperature. However, the diffraction limit of IR radiation limits traditional IR microscopy to particles > ∼10 μm, which have less relevance to aerosol health and climate impacts. Optical photothermal infrared (O-PTIR) spectroscopy is a contactless method that circumvents diffraction limitations by using changes in the scattering intensity of a continuous wave visible laser (532 nm) to detect the photothermal expansion when a vibrational mode is excited by a tunable IR laser (QCL: 800−1800 cm^{-1} or OPO: 2600−3600 cm^{-1}). Herein, we simultaneously collect O-PTIR spectra with Raman spectra at a single point for individual particles with aerodynamic diameters <400 nm (prior to impaction and spreading) at ambient temperature and pressure, by also collecting the inelastically scattered visible photons for Raman spectra. O-PTIR and Raman spectra were collected for submicrometer particles with different substrates, particle chemical compositions, and morphologies (i.e., core−shell), as well as IR mapping with submicron spatial resolution. Initial O-PTIR analysis of ambient atmospheric particles identified both inorganic and organic modes in individual sub- and supermicrometer particles. The simultaneous IR and Raman microscopy with submicrometer spatial resolution described herein has considerable potential both in atmospheric chemistry and numerous others fields (e.g., materials and biological research).

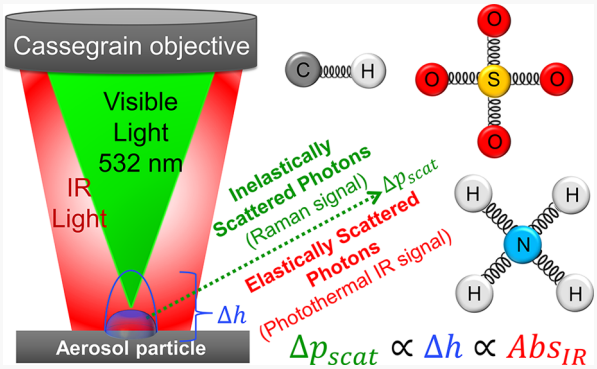

Atmospheric aerosols impact climate by scattering or absorbing solar radiation, nucleating cloud droplets and ice crystals, and undergoing heterogeneous reactions with atmospheric gases.[1] Atmospheric particles represent the largest uncertainty in the evolving radiative balance of our changing climate[1] due to their complex and evolving physicochemical properties[2−4] and the analytical challenge of measuring them.[5,6] Particles with diameters <1 μm almost always account for >99% of particles by number in the atmosphere.[1,2] Submicrometer particles are the most important contributors to the uncertain impacts of aerosols on radiative balance, and thus climate, due to their optical and cloud droplet forming properties.[1] Submicrometer particles also contribute a large fraction of fine particulate matter mass ($PM_{2.5}$, PM with aerodynamic diameters <2.5 μm), the most important size range for impacts on human health.[7,8] Inhaled submicrometer atmospheric particles deposit deep in the alveoli of the lungs, contributing significantly to pulmonary and cardiovascular diseases, and ∼8% of global deaths annually from air pollution.[9] Determining the size, chemical composition, phase state (liquid, semisolid, or solid), and structure (e.g., core−shell) of individual particles is crucial for estimating their impacts on climate and health.[10−13]

Spectroscopic methods providing both chemical and physical characterization of individual particles <1 μm under ambient conditions are limited.[5] The most common microspectroscopic methods applied to atmospheric particles have traditionally been under vacuum, such as electron microscopy with energy dispersive X-ray (EDX) spectroscopy which provides elemental information,[14−18] but limited information about organic species. Scanning transmission X-ray microscopy coupled with near edge X-ray absorption fine structure spectroscopy (STXM/NEXAFS) provides greater spectroscopic detail on carbon-containing species,[18−20] but focuses on electronic transitions and is often under vacuum, which can modify particle morphology. In contrast, vibrational spectroscopy methods (i.e., infrared (IR) and Raman) provide information on key inorganic species (e.g., sulfate, nitrate,

Received: April 7, 2020
Accepted: June 10, 2020
Published: June 10, 2020

https://dx.doi.org/10.1021/acs.analchem.0c01495
Anal. Chem. 2020, 92, 9932−9939

and ammonium) and organic functional groups present in atmospheric particles under ambient conditions.[5,21] Fourier Transform IR (FTIR) performed on bulk samples has shown the ability of vibrational spectroscopy to complement the widespread use of mass spectrometry in aerosol analysis.[22]

Raman spectroscopy has been used to study vibrational modes in individual atmospheric and laboratory-generated particles ~1 μm or larger.[19,21,23−28] To illustrate the benefits of vibrational spectroscopy for analysis of chemical species in atmospheric particles, inorganic sulfate ions (SO_4^{2-}) and organosulfates ($ROSO_3^-$) can be difficult to distinguish via aerosol mass spectrometry and other mass spectrometers using hard ionization methods,[29] but Raman clearly differentiates modes for sulfate (973 cm^{-1}), bisulfate (1040 cm^{-1}), and organosulfates (1065 cm^{-1}) in model systems,[30] particles generated in atmospheric chambers,[31] and the ambient atmosphere.[30] Recent advances to push Raman <1 μm include surface enhanced Raman spectroscopy (SERS)[32−35] and tip enhanced Raman spectroscopy (TERS),[36] but both are challenging due to inconsistent enhancements between substrates and for different vibrational modes.[35] Fluorescence emission after excitation by visible lasers provides additional challenges for the broad use of Raman spectroscopy for atmospheric particles, and is particularly challenging for primary biological, mineral dust, and soot particles, which can all fluoresce.[19,26,37]

Atomic force microscopy coupled to photothermal infrared spectroscopy (AFM-PTIR)[38] has recently been applied to study particles and their chemical properties[39−43] by providing information on vibrational modes in particles down to 100 nm diameter.[39,40] The basic principle of AFM-PTIR is that a tunable IR laser, such as an optical parametric oscillator (OPO), scans across the mid-IR (i.e., 800−3600 cm^{-1}), while an AFM tip is in contact with a particle or surface.[38,44−46] When the laser at a specific wavenumber excites a vibrational mode of a molecular species in the sample, the sample heats and slightly expands.[39,44,47] This photothermal expansion is detected by the AFM tip at each frequency as the laser source is scanned across the spectral range to produce an IR spectrum. The relationship between IR absorption and photothermal expansion detected by the AFM-PTIR tip is shown in eq 1:

$$u(t) = aG\alpha_T \Delta T(t) \tag{1}$$

where $u(t)$ is the time-dependent photothermal expansion of the sample in m^2, a is the area of the heated region in m^2 (e.g., sphere = circle = radius, cube = square = edge length), G is a geometric constant based on the shape of the sample (e.g., sphere or cube), α_T is the thermal expansion coefficient of the sample in K^{-1}, and $\Delta T(t)$ is the time-dependent temperature increase of the sample in K.[44] The thermal expansion of the sample (u) is proportional to the temperature change of the sample after absorption of incident IR radiation (ΔT), the power absorbed by the sample (P_{abs}), and the optical absorption from the Beer−Lambert Law.[44] Thus, IR absorption-like spectra are obtained by measuring the photothermal expansion of the sample as a function of wavenumber. See Dazzi and Prater for further details.[44] AFM-PTIR analysis has been time intensive; often taking 20−30 min to collect a high quality spectrum. Additionally, tip interactions, particularly during the analysis of soft or liquid samples, have been challenging.[48]

Optical photothermal infrared (O-PTIR) spectroscopy has recently been developed and overcomes both the issues of the AFM tip and slow collection time of earlier AFM-PTIR instruments.[49] With O-PTIR, localized IR absorption is obtained after coaligning a continuous wave (CW) visible laser (532 nm) and a pulsed, tunable IR laser on the sample and measuring the photothermal expansion that occurs when the incident frequency of the IR laser matches an IR absorption mode of the sample.[47,50,51] The resulting modulated photothermal expansion causes a change in the intensity of the elastically (Rayleigh) scattered light from the visible laser,[52] which can be processed to generate an IR spectrum. The photothermal response is shown in eq 2:

$$\Delta P_{PR} \propto \frac{\sigma N}{KC_p}\frac{\partial n}{\partial T} P_{pr} P_{IR} \tag{2}$$

where P_{PR} refers to the probe (visible laser) power, σ is the absorption cross section of the sample, N is the number density of absorbing molecules in the sample, K is the heat conductivity of the sample, C_p is the heat capacity of the sample, n is the refractive index of the illuminated volume of the sample, T is the temperature, and P_{IR} refers to the power of the IR laser.[49] The generated O-PTIR spectra resemble FTIR absorbance spectra.[49] Unlike traditional FTIR microscopy, O-PTIR can achieve submicron spatial resolution[67,68] because the spatial resolution is determined by the visible laser, not the longer wavelength IR laser. The potential of this new analytical technique has been shown during recent applications where O-PTIR imaged live cells,[49,53] tissues,[52] polymers,[54,55] and plasmonic nanostructures.[56]

Herein, we report simultaneous collection of O-PTIR and Raman spectra to characterize submicron atmospheric particles. As the 532 nm probe laser used for O-PTIR also generates Stokes and anti-Stokes shifted photons from inelastic scattering, these can be detected simultaneously to generate both O-PTIR and Raman spectra. The capability of O-PTIR +Raman to analyze submicrometer particles with <1 min acquisition times is shown below. Microscopy substrates were tested for optimal sample signal and to minimize interferences within OPTIR+Raman spectra. Organic and inorganic functional groups were characterized for both laboratory-generated standards and ambient aerosol particles. Mapping was performed on two-component, liquid−liquid phase-separated particles to determine the spatial distribution of chemical species. These results highlight the capability of O-PTIR to analyze particles well below the diffraction-limited spatial resolution of traditional IR microscopy and show the power of the combined O-PTIR+Raman analytical method to study physicochemical properties of atmospheric aerosol particles.

METHODS

Laboratory-Generated Aerosol Particle Samples. Standard solutions were prepared using 18.2 MΩ Milli-Q water and the following chemicals: ammonium sulfate ($(NH_4)_2SO_4$, Honeywell Fluka), ammonium nitrate (NH_4NO_3, Acros Organics), ammonium oxalate ($(NH_4)_2C_2O_4$, Sigma-Aldrich), sodium acetate (CH_3COONa, Sigma-Aldrich), sucrose ($C_{12}H_{22}O_{11}$, Fisher Scientific), polyethylene glycol (PEG 400, $C_{2n}H_{4n+2}O_{n+1}$, Honeywell Fluka), and sodium dodecyl sulfate (SDS, $NaC_{12}H_{25}SO_4$, Research Products International). All chemicals were >98% purity and used without further purification. Particles were generated by atomizing 50 mM solutions with a Collison nebulizer using HEPA-filtered air. Samples were inertially impacted onto

https://dx.doi.org/10.1021/acs.analchem.0c01495
Anal. Chem. 2020, 92, 9932−9939

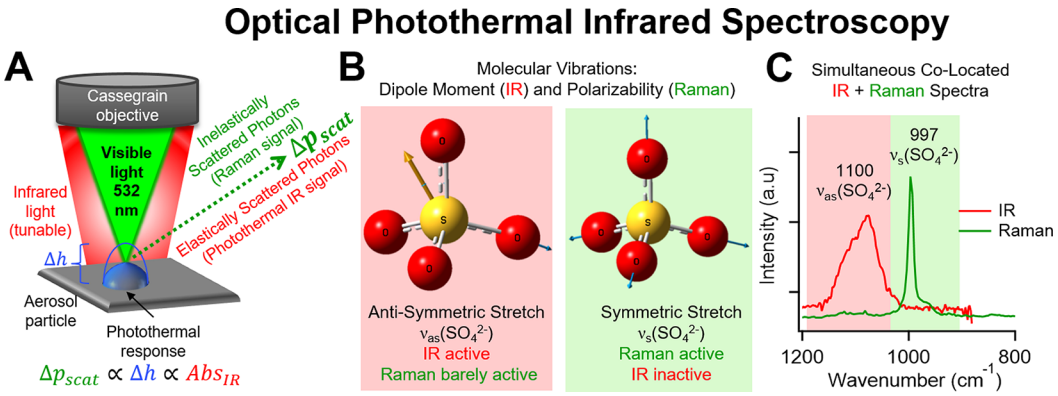

Figure 1. (A) Schematic of optical photothermal infrared spectroscopy. Infrared and visible light are focused on the sample through a Cassegrain objective, inducing a photothermal expansion of the particle. Light scattered from the sample (Δp_{scat}) is proportional to the photothermal expansion of the particle (Δh) and absorbance of IR light (Abs_{IR}). Simultaneous IR and Raman spectra are obtained from a single point. (B) Molecular vibrations are shown corresponding to antisymmetric (red) and symmetric (green) stretching modes of sulfate. (C) IR and Raman spectra obtained from a sulfate-containing particle. The peak width of $\nu_{as}(SO_4^{2-})$ is broader than $\nu_s(SO_4^{2-})$ as 3-fold degeneracy of T_d symmetry breaks down in nonideal aerosol environment.

silicon (Ted Pella Inc., product number 16013), quartz (Ted Pella Inc.), germanium (Wafer World Inc.), aluminum foil (Ted Pella Inc.), silver foil (ESPI Metals), and gold deposited onto silicon (Platypus Technologies) substrates using a microanalysis particle sampler (MPS, California Measurements Inc.). Samples impacted onto stage 3 of the MPS (<400 nm aerodynamic diameter before spreading after inertial impaction onto the substrates[39,57]) were analyzed. To provide context with respect to mass of material detected, a 400 nm particle with a 50 mM concentration of ammonium sulfate contains 160 attograms of sulfate per particle and 60 attograms of ammonium (see Supporting Information for more details). Liquid−liquid phase-separated particles were generated by atomizing a mixed solution of PEG and ammonium nitrate at a 1:1 mass ratio using 1% by weight of each compound. All samples were stored in the dark at room temperature following established protocols[58] and analyzed within 24 h at room temperature (23 °C) and relative humidity (RH, 30%). At minimum, ten particles per sample were analyzed to ensure representative and reproducible spectra, with details on the number of particles analyzed for each sample available in Supporting Information (SI) Table S1. All spectra were obtained at a single point (laser spot size ∼450 nm) in the center of particles unless otherwise stated.

Ambient Particles Sampling. Atmospheric particles were collected onto silicon substrates in Ann Arbor, MI on February 4, 2020 from 13:04−14:15 EST using an MPS. Stages 1, 2, and 3 (aerodynamic diameters of 2.8−5.0 μm, 0.4−2.8 μm, and <0.4 μm, respectively) were analyzed.

Optical Photothermal Infrared (O-PTIR) Spectroscopy. This study used a mIRage infrared + Raman microscope (Photothermal Spectroscopy Corp.) based on the O-PTIR concept of Zhang et al.,[49] which was recently utilized for polymers and fibers.[59−61] The mIRage contains a custom microscope frame with two motorized objectives: a visible objective (4 × 0.13 numerical aperture, 17.3 mm working distance, Nikon Plan Fluor) and a Cassegrain reflective objective for simultaneous use of IR and visible lasers (40 × 0.78 numerical aperture, 8.3 mm working distance, 55 μm × 42 μm field of view). The mIRage uses a CW laser source (532 nm, 200 mW, ∼20% reaches sample) as the probe (detected by a photodetector, range 0−1 mV) and two pulsed, tunable infrared lasers to generate photothermal enhancement. A quantum cascade laser (QCL) covers 880−1950 cm^{-1} with tunable repetition rate of 100 kHz, 40−500 ns pulses, up to 1 W power per pulse (much lower in practical use, see below), and four chips with spectral resolution of 2 cm^{-1}. An OPO covers the range 2700−3600 cm^{-1} with tunable repetition rate up to 150 kHz, < 10 ns pulses, > 250 mW power per pulse, and spectral resolution of 4 cm^{-1}.

Focusing was optimized for each QCL chip at 1726, 1575, 1270, and 1026 cm^{-1} using the IR signal from a polyethylene terephthalate standard within the instrument. IR spectra were collected at a scan rate of 100 cm^{-1}/s for 15 s acquisitions and averaged after three accumulations. The IR laser repetition rate was set at 100 kHz and 300 ns per pulse. The powers of the IR and visible lasers were set to approximately 4−10 mW each (details in SI and Table S2). Prior to collecting sample spectra, a background profile of the laser was collected from an AFM cantilever that absorbs uniformly at all wavenumbers in the mid-IR. The sample spectra were then divided by the background profile to produce photometrically accurate background compensated spectra across the full spectral range.

Raman Microspectroscopy. Raman scattering was detected after photons passed back through the Cassegrain objective into a Horiba iHR320 module (focal length = 320 mm) with three gratings (600, 1200, and 1800 groove/mm), spectral dispersion at 500 nm of 2.31 nm/mm, scan speed of 160 nm/sec, and step size of 0.002 nm. Spectra were collected across the spectral range of 200−4000 cm^{-1} using the 600 groove/mm grating to yield spectral resolution of 4 cm^{-1}. Raman spectra were collected using 5 s acquisitions with three accumulations and calibrated against the known Raman peaks of silicon and acetaminophen.

O-PTIR Imaging. PTIR Studio software (version 4.0, Photothermal Spectroscopy Corp.) was used to process spectra and IR images. Spectra were not smoothed and raw data is shown. IR images were generated by inputting the wavenumber of interest and scanning the field of view with 100 nm steps.[39] IR absorbance images were generated to show the intensity of IR signal on a color scale from 0−1 mV.

https://dx.doi.org/10.1021/acs.analchem.0c01495
Anal. Chem. 2020, 92, 9932−9939

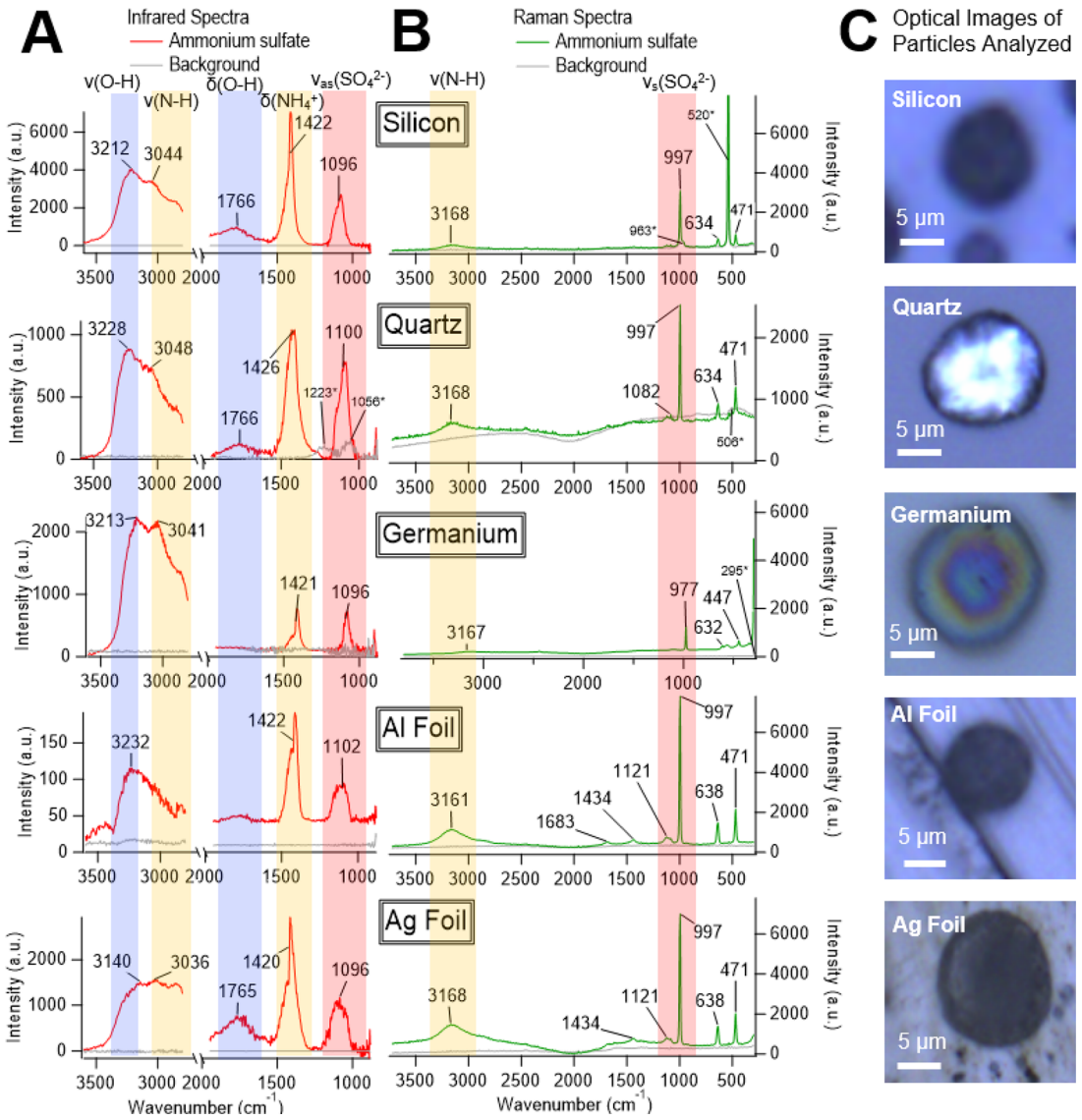

Figure 2. (A) IR and (B) Raman spectra of ammonium sulfate particles on different substrates. Background spectra were taken adjacent to the particle on a clear location of the substrate. Peaks labeled with asterisks denote contribution from the substrate and are listed in SI Table S3. Optical images of the particles analyzed are shown in panel C. All particles had aerodynamic diameters <400 nm before spreading after inertial impaction onto the substrates, with spreading ratios typically between 4:1 and 10:1.[39,57] Intensities on IR and Raman spectra are in arbitrary units, but are not related, which is also true for subsequent figures.

RESULTS AND DISCUSSION

A diagram illustrating the operating principle of O-PTIR +Raman is shown in Figure 1a. A pulsed IR laser and CW laser of 532 nm are coaligned and focused through a Cassegrain objective onto the sample. If the vibrational energy levels of the sample match the incident frequency of IR light, IR light is absorbed by the sample (Abs_{IR}) leading to photothermal expansion (Δh) and change in refractive index based on the heat capacity (C_p), heat conductivity (K), and absorption cross section of the sample(σ).[49,52,62] SI Table S2 includes available values for the compounds used. The change in scattering (Δp_{scat}) due to changes in refractive index with temperature and photothermal expansion is detected and extracted to give an IR spectrum of the sample.[49,52,62] The inelastically scattered photons from the sample pass back through the Cassegrain objective to a Raman spectrometer. With O-PTIR+Raman, we are able to observe molecular vibrations associated with changes in the dipole moment (IR) and polarizability (Raman) of the species analyzed. The ability to detect both IR active and Raman active vibrational modes simultaneously from the same spot and with the same submicron spatial resolution allows for far more comprehensive sample characterization. As an example, we show the symmetric and antisymmetric stretching modes of sulfate molecules (Figure 1b) with the corresponding spectra generated from an ammonium sulfate particle (Figure 1c). $\nu_s(SO_4^{2-})$ is not IR active as the dipole moment of this symmetric molecule does not change during this molecular vibration, however, the polarizability does, making it Raman active. There is a substantial dipole moment change for $\nu_{as}(SO_4^{2-})$ that corresponds to intense signal in the IR spectrum, but the Raman activity of $\nu_{as}(SO_4^{2-})$ is weaker. Thus, by obtaining both IR and Raman spectra at the same point simultaneously, greater molecular detail can be obtained for a wide range of samples.

Optimal substrates for both spectroscopies need to be determined as IR and Raman spectra have seldom been

https://dx.doi.org/10.1021/acs.analchem.0c01495
Anal. Chem. 2020, 92, 9932−9939

collected simultaneously, particularly not from the same spot and with the same spatial resolution. Interferences for different substrates were explored by impacting ammonium sulfate particles onto common microscopy substrates including silicon, quartz, germanium, aluminum foil, silver foil, and Platypus flat gold. IR vibrational modes observed include $\nu_{as}(SO_4^{2-})$ at 1100 cm^{-1}, $\delta(NH_4^+)$ at 1422 cm^{-1}, ν(N−H) at ∼3040 cm^{-1}, with δ(O−H) at 1766 cm^{-1} and ν(O−H) at ∼3220 cm^{-1} from water (Figure 2A). Ammonium sulfate modes are comparable to FTIR spectra of ammonium sulfate (SI Figure S1).[39,40,63] Raman spectra contained peaks at 977 cm^{-1} representing $\nu_s(SO_4^{2-})$, 634 cm^{-1} for an umbrella bend $\delta(SO_4^{2-})$, 471 cm^{-1} representing a scissoring motion for SO_4^{2-}, and ∼3168 cm^{-1} representing ν(N−H) (Figure 2B).[21,28,31,64] Optical images of each particle are shown in Figure 2C, with images of blank substrates and peaks from substrates listed in SI Table S3. Fluorescence was generated with flat gold substrates, which overwhelmed the Raman signal of the sample (SI Figure S2). Al foil provided weak IR signal, possibly due to the rough surface. Quartz showed interference peaks in the IR spectra at 1056 and 1223 cm^{-1} and an uneven baseline in the Raman spectra. While germanium and Ag foil had minimal spectral interferences, the IR signal generated from particles on these substrates was lower than with silicon. Silicon was determined to be the best substrate and was used hereafter due to minimal interference in the Raman spectra (520 and 963 cm^{-1}), no interference in the IR spectra, and intense sample signal compared to other substrates tested.

Aerosols from single-component solutions were used to evaluate the ability of O-PTIR to study a range of species commonly observed in atmospheric particles. Representative IR and Raman spectra of laboratory-generated particles (ammonium nitrate, sodium acetate, sucrose, SDS, and ammonium oxalate) on silicon substrates are shown in Figure 3, with spectral assignments and corresponding references reported in SI Table S4. Optical images of all particles analyzed are shown in SI Figure S3. The combined O-PTIR+Raman spectra clearly distinguish organic and inorganic vibrational modes commonly found in atmospheric particles.

Ambient particles were analyzed with O-PTIR+Raman for the first time. Particles containing ammonium nitrate were identified by IR modes at 1351 and 1411 cm^{-1}, indicative of $\nu_a(NO_3^-)$ and $\delta(NH_4^+)$, respectively (Figure 4A).[39,65] The same particle contained Raman modes at 1068 and ∼3150 cm^{-1}, representing $\nu(NO_3^-)$ and ν(N−H), respectively.[21,23,34] The agreement between IR and Raman provide robust evidence for the presence of ammonium nitrate, much stronger than either IR or Raman would provide independently due to common peaks in similar regions (e.g., organosulfates ∼1065 cm^{-1} in Raman).[30,31] Similarly, ambient sulfate-containing particles were identified by $\nu_{as}(SO_4^{2-})$ at 1107 cm^{-1} in the IR spectrum[39,63] and $\nu_s(SO_4^{2-})$ at 990 cm^{-1} in the Raman spectrum (Figure 4C).[21,31,64] This particle also contained organic modes identified as δ(C−H) in the IR spectrum[66] and ν(C−H), $\nu(CH_2)$, and $\delta(CH_2)$ in the Raman spectrum,[67,68] similar to mixtures of sulfate and organic material identified in ambient particles with AFM-PTIR[39,43,69] and Raman.[19,28,34] Additional organic vibrational modes were identified in both IR and Raman spectra of ambient particles (Figure 4B), resembling modes detected in oxalate,[70] sucrose,[68] and SDS[24,66] (Figure 3). OPTIR+Raman spectra show that significant chemical detail can be obtained from atmospheric particles containing complex mixtures of chemical species.[6]

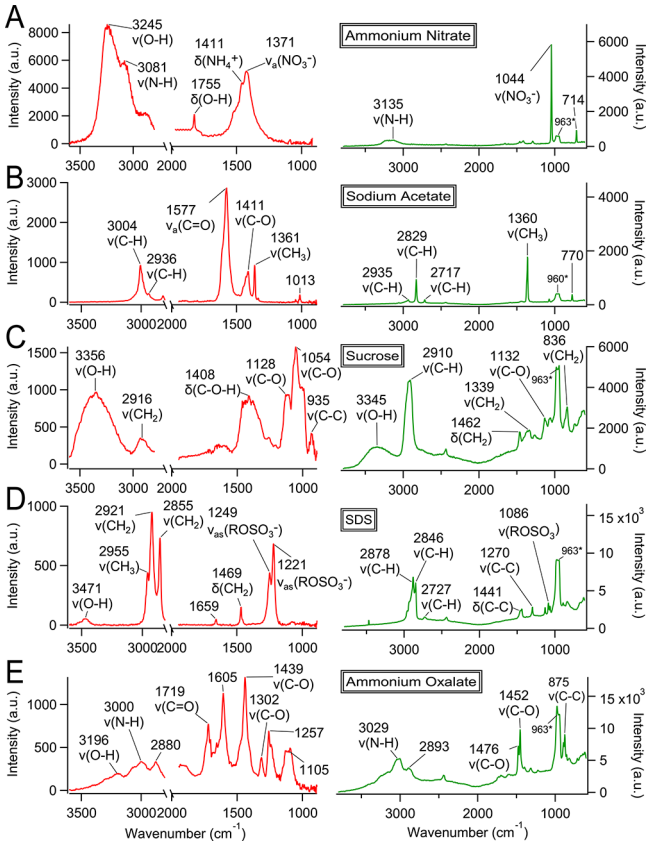

Figure 3. IR (left, red trace) and Raman (right, green trace) spectra of (A) ammonium nitrate, (B) sodium acetate, (C) sucrose, D) SDS, and (E) ammonium oxalate particles. Peaks labeled with * in the Raman spectra indicate contribution from the silicon substrate. All particles had an aerodynamic diameter <400 nm before spreading after inertial impaction onto the silicon substrates.

Atmospheric particles are frequently not homogeneous, but rather adopt core−shell and other complicated morphologies.[11,69,71] To demonstrate the spatial distribution of chemical species within an individual particle, IR spectra and maps were collected from liquid−liquid phase-separated particles containing PEG and ammonium nitrate with aerodynamic diameters <400 nm, which spread upon impaction. A line scan (Figure 5A) collected spectra every 2.0 μm across a two-component, phase-separated particle. IR spectra collected from the core and shell of the particle confirm the presence of nitrate primarily in the particle core and PEG primarily in the particle shell (Figure 5A). The IR peak intensity ratio of 1105 and 1371 cm^{-1}, corresponding to ν(C−O)[39] and $\nu_a(NO_3^-)$,[39] respectively, was calculated at each point in the line scan to show the enhancement of PEG on the edge of the particle with minimal PEG in the particle core (Figure 5B). Two IR modes representing ν(C−O)[39] and $\nu_a(NO_3^-)$[39] (1105 and 1371 cm^{-1}, respectively) were observed with differing spatial distributions in spectral maps with 100 nm step sizes (Figure 5C). Inorganic components (nitrate) were located primarily in the core of the particle, while the outer layer of the particle was primarily organic (PEG), similar to previously observed phase-separated particles studied in the laboratory[31,40,71] and in ambient environments.[69] These results show that O-PTIR can determine the distribution of chemical species within individual particles related to particle morphology, which can be used to study aerosol physicochemical mixing state.[6]

https://dx.doi.org/10.1021/acs.analchem.0c01495
Anal. Chem. 2020, 92, 9932−9939

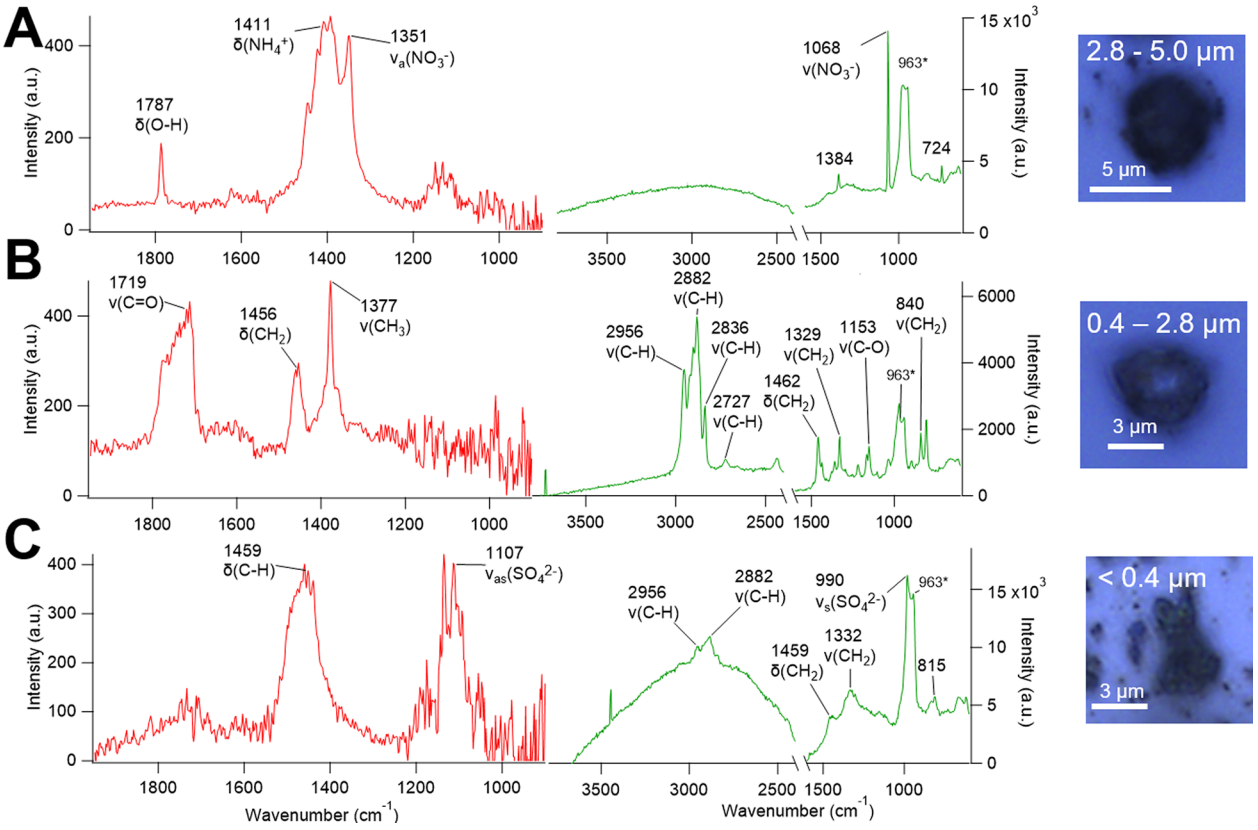

Figure 4. IR (left, red trace) and Raman (right, green trace) spectra obtained from ambient (A) ammonium nitrate-containing, (B) organic, and (C) organic- and sulfate-containing particles. Peaks corresponding to vibrational modes identified from laboratory-generated standards are labeled. Peaks labeled with * in the Raman spectra indicate contribution from the silicon substrate. Optical images of each particle analyzed are shown on the right and are labeled with the size range of the impactor stage on which the particle was collected. Uneven baselines in the Raman spectra are likely from fluorescence.

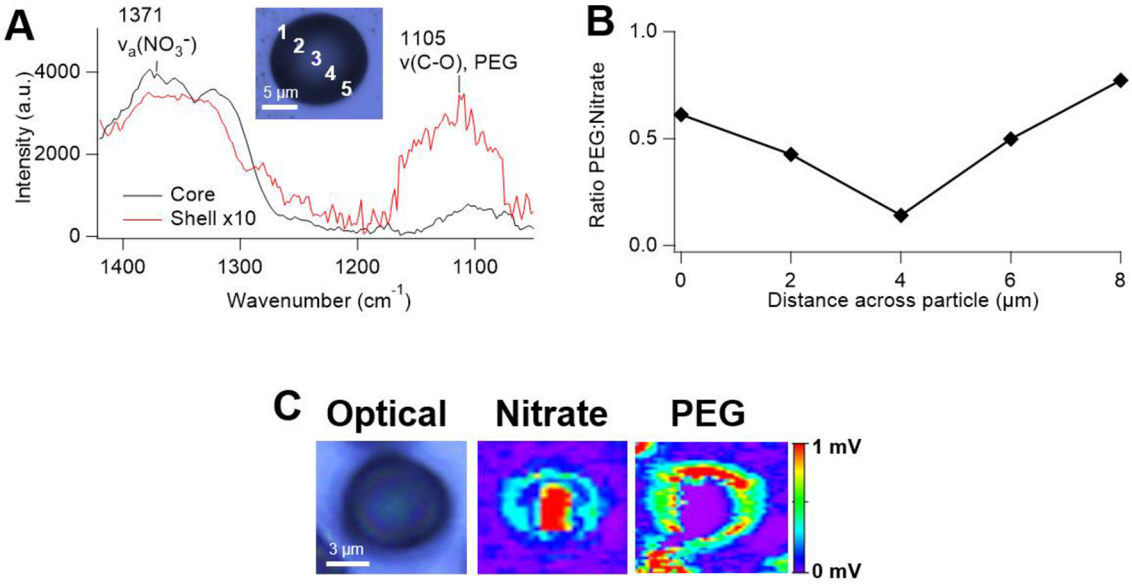

Figure 5. (A) IR spectra collected from the core (point 3 on the line scan) and shell (point 1) of phase-separated PEG + ammonium nitrate particle. Shell spectra was multiplied 10× for clarity. The optical image of the particle analyzed includes numbers denoting the location of the five spectra acquired during the line scan. (B) Ratio of the intensity of PEG and nitrate IR peaks obtained during the line scan, confirming the presence of PEG primarily in the outer shell of the particle with nitrate in the core. (C) Optical image of phase-separated PEG + ammonium nitrate particle, with maps showing the location of nitrate (1371 cm^{-1}) in the core of the particle and PEG (1105 cm^{-1}) in the outer shell using 100 nm step size. It should be noted that repeating scans (2 or more) across the sample resulted in minor beam damage to organic compounds and is visible through the slightly irregularly shaped shell.

https://dx.doi.org/10.1021/acs.analchem.0c01495
Anal. Chem. 2020, 92, 9932−9939

CONCLUSIONS

The simultaneous spectroscopic and physicochemical analysis of submicron aerosol particles is analytically challenging because traditional vibrational spectroscopy techniques, such as FTIR, struggle to investigate particles in the size range reported herein (<400 nm aerodynamic diameter before spreading after impaction onto the substrates) as the diffraction limit of IR light traditionally limits spatial resolution. O-PTIR+Raman was applied to simultaneously collect vibrational IR and Raman spectra from individual particles <400 nm aerodynamic diameter under ambient conditions, allowing for faster analysis times and complementary chemical information. We show the potential of O-PTIR+Raman for single-component model systems, two-component phase-separated particles, and ambient aerosol particles. The contactless nature of O-PTIR enables analysis of different phase states (liquid, semisolid, or solid).[31,69,72] High spatial resolution maps of vibrational modes presented within particles demonstrate the ability of this analytical technique to determine intraparticle chemical differences, which impact aerosol reactivity in the atmosphere.[72] Future work will push the analytical capabilities of O-PTIR to even smaller particles, with a focus on viscous particles that spread less upon impaction and ambient particles whose viscosity changes as a function of RH and temperature. Spectral information obtained will enable key insights regarding physicochemical properties of atmospheric particles in a critical size range for climate and human health. The power of O-PTIR+Raman, shown above for laboratory-generated and atmospheric particles, has applications for a wide range of scientific disciplines from materials science to the biosciences.

ASSOCIATED CONTENT

Supporting Information

The Supporting Information is available free of charge at https://pubs.acs.org/doi/10.1021/acs.analchem.0c01495.

> Number of particles analyzed for each substrate and compound, table with heat capacity, heat conductivity, refractive index, and laser power of analyzed chemicals, IR and Raman spectra of ammonium sulfate crystals, table of IR and Raman peaks and optical images of tested substrates, IR and Raman spectra of ammonium sulfate particles on Platypus gold substrate, table of assigned vibrational modes for Figure 3 particles, and optical images of Figure 3 particles (PDF)

AUTHOR INFORMATION

Corresponding Author

Andrew P. Ault − *Department of Chemistry, University of Michigan, Ann Arbor, Michigan 48109, United States;* orcid.org/0000-0002-7313-8559; Email: aulta@umich.edu

Authors

Nicole E. Olson − *Department of Chemistry, University of Michigan, Ann Arbor, Michigan 48109, United States;* orcid.org/0000-0003-1600-8050

Yao Xiao − *Department of Chemistry, University of Michigan, Ann Arbor, Michigan 48109, United States;* orcid.org/0000-0003-3661-2845

Ziying Lei − *Department of Environmental Health Sciences, University of Michigan, Ann Arbor, Michigan 48109, United States;* orcid.org/0000-0003-3071-0698

Complete contact information is available at: https://pubs.acs.org/10.1021/acs.analchem.0c01495

Notes

The authors declare no competing financial interest.

ACKNOWLEDGMENTS

We thank Sergey Zayats, Eoghan Dillon, and the Photothermal Spectroscopy Corp. team for instrument training and helpful discussions regarding data interpretation. Funding for this project was provided by National Science Foundation CAREER Grant CHE-1654149, Alfred P. Sloan Foundation Research Fellowship (Chemistry) G-2018-11239, and the Department of Chemistry at the University of Michigan.

REFERENCES

(1) Seinfeld, J. H.; Pandis, S. N. *Atmospheric chemistry and physics: from air pollution to climate change*. John Wiley & Sons: 2016.

(2) Bauer, S. E.; Ault, A.; Prather, K. A. *J. Geophys. Res.: Atmos.* **2013**, *118* (17), 9834−9844.

(3) Fitzgerald, E.; Ault, A. P.; Zauscher, M. D.; Mayol-Bracero, O. L.; Prather, K. A. *Atmos. Environ.* **2015**, *115*, 19−25.

(4) Riva, M.; Chen, Y.; Zhang, Y.; Lei, Z.; Olson, N.; Boyer, H. C.; Narayan, S.; Yee, L. D.; Green, H.; Cui, T.; Zhang, Z.; Baumann, K. D.; Fort, M.; Edgerton, E. S.; Budisulistiorini, S.; Rose, C. A.; Ribeiro, I.; e Oliveira, R. L.; Santos, E.; Szopa, S.; Machado, C.; Zhao, Y.; Alves, E.; de Sa, S.; Hu, W.; Knipping, E.; Shaw, S.; Duvoisin Junior, S.; Souza, R. A. F. d.; Palm, B. B.; Jimenez, J. L.; Glasius, M.; Goldstein, A. H.; Pye, H. O. T.; Gold, A.; Turpin, B. J.; Vizuete, W.; Martin, S. T.; Thornton, J.; Dutcher, C. S.; Ault, A. P.; Surratt, J. D. *Environ. Sci. Technol.* **2019**, *53* (15), 8682−8694.

(5) Ault, A.; Axson, J. *Anal. Chem.* **2017**, *89*, 430−452.

(6) Riemer, N.; Ault, A. P.; West, M.; Craig, R. L.; Curtis, J. H. *Rev. Geophys.* **2019**, *57*, 187−249.

(7) Dedoussi, I. C.; Eastham, S. D.; Monier, E.; Barrett, S. R. H. *Nature* **2020**, *578* (7794), 261−265.

(8) Pope, C. A.; Dockery, D. W. *J. Air Waste Manage. Assoc.* **2006**, *56* (6), 709−742.

(9) Institute for Health Metrics and Evaluation - IHME. Global Burden of Disease Compare Data Visualization, Seattle, WA, 2016.

(10) Fierce, L.; Bond, T. C.; Bauer, S. E.; Mena, F.; Riemer, N. *Nat. Commun.* **2016**, *7*, 12361.

(11) Freedman, M. A. *Chem. Soc. Rev.* **2017**, *46*, 7694−7705.

(12) Virtanen, A.; Joutsensaari, J.; Koop, T.; Kannosto, J.; Yli-Pirila, P.; Leskinen, J.; Makela, J. M.; Holopainen, J. K.; Poschl, U.; Kulmala, M.; Worsnop, D. R.; Laaksonen, A. *Nature* **2010**, *467* (7317), 824−827.

(13) Eaves, L. A.; Smeester, L.; Hartwell, H. J.; Lin, Y.-H.; Arashiro, M.; Zhang, Z.; Gold, A.; Surratt, J. D.; Fry, R. C. *Chem. Res. Toxicol.* **2020**, *33* (2), 381−387.

(14) Shen, H.; Peters, T. M.; Casuccio, G. S.; Lersch, T. L.; West, R. R.; Kumar, A.; Kumar, N.; Ault, A. P. *Environ. Sci. Technol.* **2016**, *50* (10), 4961−4970.

(15) Bondy, A. L.; Bonanno, D.; Moffet, R. C.; Wang, B.; Laskin, A.; Ault, A. P. *Atmos. Chem. Phys.* **2018**, *18* (16), 12595−12612.

(16) Bondy, A. L.; Wang, B.; Laskin, A.; Craig, R. L.; Nhliziyo, M. V.; Bertman, S. B.; Pratt, K. A.; Shepson, P. B.; Ault, A. P. *Environ. Sci. Technol.* **2017**, *51*, 9533−9542.

(17) Laskin, A.; Iedema, M. J.; Cowin, J. P. *Environ. Sci. Technol.* **2002**, *36* (23), 4948−4955.

(18) Ault, A. P.; Moffet, R. C.; Baltrusaitis, J.; Collins, D. B.; Ruppel, M. J.; Cuadra-Rodriguez, L. A.; Zhao, D.; Guasco, T. L.; Ebben, C. J.; Geiger, F. M.; Bertram, T. H.; Prather, K. A.; Grassian, V. H. *Environ. Sci. Technol.* **2013**, *47* (11), 5603−5612.

(19) Kirpes, R. M.; Bonanno, D.; May, N. W.; Fraund, M.; Barget, A. J.; Moffet, R. C.; Ault, A. P.; Pratt, K. A. *ACS Cent. Sci.* **2019**, *5*, 1760−1767.
(20) O'Brien, R. E.; Wang, B.; Kelly, S. T.; Lundt, N.; You, Y.; Bertram, A. K.; Leone, S. R.; Laskin, A.; Gilles, M. K. *Environ. Sci. Technol.* **2015**, *49* (8), 4995−5002.
(21) Craig, R. L.; Bondy, A. L.; Ault, A. P. *Aerosol Sci. Technol.* **2017**, *51*, 1099−1112.
(22) Takahama, S.; Johnson, A.; Russell, L. M. *Aerosol Sci. Technol.* **2013**, *47* (3), 310−325.
(23) Craig, R. L.; Nandy, L.; Axson, J. L.; Dutcher, C. S.; Ault, A. P. *J. Phys. Chem. A* **2017**, *121* (30), 5690−5699.
(24) Ault, A. P.; Zhao, D.; Ebben, C. J.; Tauber, M. J.; Geiger, F. M.; Prather, K. A.; Grassian, V. H. *Phys. Chem. Chem. Phys.* **2013**, *15* (17), 6206−6214.
(25) Ebben, C. J.; Ault, A. P.; Ruppel, M. J.; Ryder, O. S.; Bertram, T. H.; Grassian, V. H.; Prather, K. A.; Geiger, F. M. *J. Phys. Chem. A* **2013**, *117* (30), 6589−6601.
(26) Doughty, D. C.; Hill, S. C. *J. Quant. Spectrosc. Radiat. Transfer* **2020**, *244*, 106839.
(27) Doughty, D. C.; Hill, S. C. *J. Quant. Spectrosc. Radiat. Transfer* **2017**, *188*, 103−117.
(28) Kirpes, R. M.; Bondy, A. L.; Bonanno, D.; Moffet, R. C.; Wang, B.; Laskin, A.; Ault, A. P.; Pratt, K. A. *Atmos. Chem. Phys.* **2018**, *18* (6), 3937−3949.
(29) Farmer, D.; Matsunaga, A.; Docherty, K.; Surratt, J.; Seinfeld, J.; Ziemann, P.; Jimenez, J. *Proc. Natl. Acad. Sci. U. S. A.* **2010**, *107* (15), 6670−6675.
(30) Bondy, A. L.; Craig, R. L.; Zhang, Z.; Gold, A.; Surratt, J. D.; Ault, A. P. *J. Phys. Chem. A* **2018**, *122* (1), 303−315.
(31) Olson, N. E.; Lei, Z.; Craig, R. L.; Zhang, Y.; Chen, Y.; Lambe, A. T.; Zhang, Z.; Gold, A.; Surratt, J. D.; Ault, A. P. *ACS Earth Space Chem.* **2019**, *3*, 1402−1414.
(32) Gen, M.; Chan, C. K. *Atmos. Chem. Phys.* **2017**, *17* (22), 14025−14037.
(33) Fu, Y.; Kuppe, C.; Valev, V. K.; Fu, H.; Zhang, L.; Chen, J. *Environ. Sci. Technol.* **2017**, *51* (11), 6260−6267.
(34) Craig, R. L.; Bondy, A. L.; Ault, A. P. *Anal. Chem.* **2015**, *87* (15), 7510−7514.
(35) Tirella, P. S.; Craig, R. L.; Tubbs, D. B.; Olson, N. E.; Lei, Z.; Ault, A. P. *Environ. Sci.: Processes Impacts* **2018**, *20*, 1570−1580.
(36) Ofner, J.; Deckert-Gaudig, T.; Kamilli, K. A.; Held, A.; Lohninger, H.; Deckert, V.; Lendl, B. *Anal. Chem.* **2016**, *88* (19), 9766−9772.
(37) Creamean, J. M.; Axson, J. L.; Bondy, A. L.; Craig, R. L.; May, N. W.; Shen, H.; Weber, M. H.; Pratt, K. A.; Ault, A. P. *J. Geophys. Res. Atmos.* **2016**, *121*, 7296−7309.
(38) Dazzi, A.; Prater, C. B.; Hu, Q.; Chase, D. B.; Rabolt, J. F.; Marcott, C. *Appl. Spectrosc.* **2012**, *66* (12), 1365−1384.
(39) Bondy, A. L.; Kirpes, R. M.; Merzel, R. L.; Pratt, K. A.; Banaszak Holl, M. M.; Ault, A. P. *Anal. Chem.* **2017**, *89*, 8594−8598.
(40) Or, V. W.; Estillore, A.; Grassian, V.; Tivanski, A. V. *Analyst* **2018**, *143* (12), 2765−2774.
(41) Wang, L.; Huang, D.; Chan, C. K.; Li, Y. J.; Xu, X. G. *Chem. Commun.* **2017**, *53* (53), 7397−7400.
(42) Lei, Z.; Bliesner, S. E.; Mattson, C. N.; Cooke, M. E.; Olson, N. E.; Chibwe, K.; Albert, J. N. L.; Ault, A. P. *Anal. Chem.* **2020**, *92* (9), 6502−6511.
(43) Kirpes, R. M.; Rodriguez, B.; Kim, S.; China, S.; Laskin, A.; Park, K.; Jung, J.; Ault, A. P.; Pratt, K. A. *Environ. Sci. Process Impacts* **2020**, *22* (5), 1201−1213.
(44) Dazzi, A.; Prater, C. B. *Chem. Rev.* **2017**, *117*, 5146−5173.
(45) Kurouski, D.; Dazzi, A.; Zenobi, R.; Centrone, A. *Chem. Soc. Rev.* **2020**, *49* (11), 3315−3347.
(46) Morsch, S.; Lyon, S. B.; Edmondson, S.; Gibbon, S. R. *Anal. Chem.* **2020**, *92* (12), 8117−8124, DOI: 10.1021/acs.analchem.9b05793.
(47) Dazzi, A.; Glotin, F.; Carminati, R. *J. Appl. Phys.* **2010**, *107*, 124519.
(48) Mathurin, J.; Pancani, E.; Deniset-Besseau, A.; Kjoller, K.; Prater, C. B.; Gref, R.; Dazzi, A. *Analyst* **2018**, *143* (24), 5940−5949.
(49) Zhang, D.; Li, C.; Zhang, C.; Slipchenko, M. N.; Eakins, G.; Cheng, J.-X. *Sci. Adv.* **2016**, *2* (9), No. e1600521.
(50) Busse, G. *Opt. Commun.* **1981**, *36* (6), 441−443.
(51) Wang, C. T.; Jiang, B.; Zhou, Y. W.; Jiang, T. W.; Liu, J. H.; Zhu, G. D.; Cai, W. B. *Anal. Chem.* **2019**, *91* (16), 10541−10548.
(52) Wrobel, T. P.; Bhargava, R. *Anal. Chem.* **2018**, *90* (3), 1444−1463.
(53) Li, X.; Zhang, D.; Bai, Y.; Wang, W.; Liang, J.; Cheng, J. X. *Anal. Chem.* **2019**, *91* (16), 10750−10756.
(54) Nowak, D.; Morrison, W.; Wickramasinghe, H. K.; Jahng, J.; Potma, E.; Wan, L.; Ruiz, R.; Albrechy, T. R.; Schmidt, K.; Frommer, J.; Sanders, D. P.; Park, S. *Sci. Adv.* **2016**, *2*, No. e1501571.
(55) Jahng, J.; Fishman, D. A.; Park, S.; Nowak, D. B.; Morrison, W. A.; Wickramasinghe, H. K.; Potma, E. O. *Acc. Chem. Res.* **2015**, *48* (10), 2671−2679.
(56) Tumkur, T. U.; Yang, X.; Cerjan, B.; Halas, N. J.; Nordlander, P.; Thomann, I. *Nano Lett.* **2016**, *16* (12), 7942−7949.
(57) Sobanska, S.; Falgayrac, G.; Rimetz-Planchon, J.; Perdrix, E.; Brémard, C.; Barbillat, J. *Microchem. J.* **2014**, *114*, 89−98.
(58) Laskina, O.; Morris, H. S.; Grandquist, J. R.; Estillore, A. D.; Stone, E. A.; Grassian, V. H.; Tivanski, A. V. *Environ. Sci. Technol.* **2015**, *49* (22), 13447−13453.
(59) Marcott, C.; Kansiz, M.; Dillon, E.; Cook, D.; Mang, M. N.; Noda, I. *J. Mol. Struct.* **2020**, *1210*, 128045.
(60) Klementieva, O.; Sandt, C.; Martinsson, I.; Kansiz, M.; Gouras, G. K.; Borondics, F. *Adv. Sci.* **2020**, *7*, 1903004.
(61) Hale, R. C.; Seeley, M. E.; La Guardia, M. J.; Mai, L.; Zeng, E. Y., A global perspective on microplastics. *J. Geophys. Res.: Oceans* **2020**, *125*, (1). DOI: 10.1029/2018JC014719
(62) Furstenberg, R.; Kendziora, C.; Papantonakis, M.; Nguyen, V.; McGill, R. A. *Chemical Imaging Using Infrared Photothermal Microspectroscopy*; SPIE, 2012; Vol. *8374*.
(63) Onasch, T. B.; Siefert, R. L.; Brooks, S. D.; Prenni, A. J.; Murray, B.; Wilson, M. A.; Tolbert, M. A. *J. Geophys Res. Atmos* **1999**, *104*, 21317−21326.
(64) Rindelaub, J. D.; Craig, R. L.; Nandy, L.; Bondy, A. L.; Dutcher, C. S.; Shepson, P. B.; Ault, A. P. *J. Phys. Chem. A* **2016**, *120* (6), 911−917.
(65) Theoret, A.; Sandorfy, C. *Can. J. Chem.* **1964**, *42*, 57−62.
(66) Gao, X.; Chorover, J. *J. Colloid Interface Sci.* **2010**, *348* (1), 167−176.
(67) Wang, L. Y.; Zhang, Y. H.; Zhao, L. J. *J. Phys. Chem. A* **2005**, *109*, 609−614.
(68) Brizuela, A. B.; Bichara, L. C.; Romano, E.; Yurquina, A.; Locatelli, S.; Brandan, S. A. *Carbohydr. Res.* **2012**, *361*, 212−218.
(69) Slade, J. H.; Ault, A. P.; Bui, A. T.; Ditto, J. C.; Lei, Z.; Bondy, A. L.; Olson, N. E.; Cook, R. D.; Desrochers, S. J.; Harvey, R. M.; Erickson, M. H.; Wallace, H. W.; Alvarez, S. L.; Flynn, J. H.; Boor, B. E.; Petrucci, G. A.; Gentner, D. R.; Griffin, R. J.; Shepson, P. B. *Environ. Sci. Technol.* **2019**, *53*, 4977−4987.
(70) Frost, R. L.; Jing, Y.; Ding, Z. *Chin. Sci. Bull.* **2003**, *48* (17), 1844−1852.
(71) Veghte, D. P.; Altaf, M. B.; Freedman, M. A. *J. Am. Chem. Soc.* **2013**, *135* (43), 16046−16049.
(72) Zhang, Y.; Chen, Y.; Lei, Z.; Olson, N. E.; Riva, M.; Koss, A. R.; Zhang, Z.; Gold, A.; Jayne, J. T.; Worsnop, D. R.; Onasch, T. B.; Kroll, J. H.; Turpin, B. J.; Ault, A. P.; Surratt, J. D. *ACS Earth Space Chem.* **2019**, *3* (12), 2646−2658.

https://dx.doi.org/10.1021/acs.analchem.0c01495
Anal. Chem. 2020, 92, 9932−9939